J. Fluid Mech. (1993), *vol.* 253, *pp.* 27–43

Characteristics of the vortex wave

By BRUCE M. DEBLOIS[1]†, IAN J. SOBEY[1] AND SAAD ALANI[2]‡

[1] Computing Laboratory, Oxford University, Oxford OX1 3QD, UK

[2] Department of Engineering Science, Oxford University, Oxford OX1 3PJ, UK

(Received 21 October 1992)

The generation of a standing wave of vortices in thin channels has been experimentally observed and discussed in the literature for the last several years. The specific cause of the wave and its response to various conditions remains largely unexplored. In this paper we model pulsatile flow through thin channels with inserted deflectors to generate the vortex wave, and we examine various measures to quantify its effects. We focus on the numerical solution of the transient vortex wave phenomenon and its response to a superimposed bulk flow, variations of pulsation, deflector spacing and shape as well as transverse suction. The quantifying measures are mapped over a Reynolds' number–Strouhal number domain.

1. Introduction

In this paper we consider calculations of some characteristics of a vortex wave and illustrate the potential use of a vortex wave mechanism in mixing or filtration processes. Stephanoff *et al.* (1983) first observed a vortex wave during steady flow past a moving indentation and Sobey (1985) showed that a vortex wave would also form downstream of a channel expansion during oscillatory flow. Separation occurs in the lee of the channel expansion, forming a primary vortex on the wall of the expanded side of the channel. At the end of the acceleration phase, the centre of the primary vortex is observed to be further downstream than in the case of steady flow, and the unsteadiness also produces a substantial secondary vortex further downstream on the opposite wall. During the deceleration phase of the oscillatory flow (which causes a reverse pressure gradient throughout the channel), both primary and secondary vortices shrink and move upstream, while further alternating vortices become apparent. The core flow acts as a wave between these vortices. The vortices do not move downstream, they remain in place and increase in intensity as flow deceleration continues. At zero flow, the waving core flow disappears and the residual vortices remain, although falling off in intensity. Upon flow reversal, these residual vortices are washed away and the cycle of the wave is reinitiated in the opposite direction. Later in this paper we will also address whether the vortices force the core flow to appear as a wave, or whether a genuine waving core flow drives the vortices. The main feature of a vortex wave which needs emphasizing is that it is a two-dimensional standing wave formed during the deceleration period wherein the core flow follows a sinuous path with a sequence of vortices forming alternately on each wall between the core flow and the walls of the channel.

Computations of the case of a vortex wave formed during steady flow past a moving indentation were carried out by Ralph & Pedley (1988). Sobey (1985) also reported

† Current address: USAF Academy, CO 80840, USA.

‡ Current address: Biwater Treatment Ltd, Gregge St, Heywood OL10 2DX, UK.

both experimental observations and calculations of unsteady flow past a fixed indentation. Other calculations of unsteady flow past a fixed channel expansion can be found in Tutty & Pedley (1992). These last two papers used a finite-difference discretization of the equations of motion. In this paper we present results of computations using a finite-element method and primitive variables. Our discritization in time is semi-implicit and spatially we use quadratic triangular elements within a Galerkin-weighted-residuals formulation. The numerical technique is described in detail in DeBlois (1991) and DeBlois & Sobey (1992). This numerical method has proven robust and produced results which compare closely to the experimental results of Sobey (1985) as well as providing new results about the vortex wave.

The formation of a sequence of vortices is not only an interesting fluid dynamic phenomenon, it can also be adapted to practical problems associated with mixing and filtration. If steady flow through a parallel channel is used to provide mass transfer through the channel walls then the formation of concentration boundary layers at the walls results in a degradation in the performance of the device with time. The use of convective mixing to overcome problems caused by these wall layers is well established (Bellhouse & Lewis 1988). It is clear that oscillatory flow can play a central role in efficiently disrupting wall layers and in providing a mechanism for interchange of material between the core of a channel flow and regions adjacent to the channel walls. Previous pulsatile flow devices have relied on using a single vortex in a furrow or dimple pressed into a membrane which makes up the channel wall. In the case of a vortex wave it is clear that a sequence of flow obstructions placed adjacent to the walls would provide a means whereby a vortex wave can form during each half-cycle of flow. If the flow deflectors are placed alternately on opposite walls then some of the energy remaining in the rotating vortices at the end of one half-cycle will augment that available from the main pulsation in the initial phase of the next half-cycle and the mixing performance should be greatest when the spacing between obstructions is tuned to the wavelength of the vortices. In order to demonstrate the application of a vortex wave mechanism to mixing processes we consider the mixing *chamber* which would occur between two obstructions placed adjacent to opposite walls and calculate the vortex wave which forms within this chamber. The resulting flows compare very closely with the flows that occur in the absence of a downstream obstruction.

In both flow past a backward-facing step and flow in a mixing chamber the vortex wave which forms can be examined in detail from the computed numerical solution. A number of interesting features emerge. Calculations of the wavelength of the vortex wave lend considerable support to the theories of Pedley & Stephanoff (1985) and Sobey (1985) that the vortex wave is dominated by an inviscid deformation of vorticity in the oncoming flow. These calculations also show that under some circumstances the vortex wave has associated with it two different wavelengths. These are a longer one in accordance with inviscid rotational deformation theory in the immediate lee of the expansion, and a shorter one in the parallel part of the channel further downstream. Vortex motion is associated with both wavelengths. Re-examination of some of the results presented in Sobey (1985, figures 10 and 11) appear to confirm this hitherto unnoticed feature of the vortex wave. We are also able to calculate vortex splitting, a feature discussed by Pedley & Stephanoff (1985). Our results show that vortex splitting appears to be a rapid transient within the period of growth and decay of the main vortex wave.

Visualization of the flow results is accomplished using velocity vectors scaled to emulate pictures of particle traces taken by a camera with shutter speed $\frac{1}{120}$th of a second. Although in some of the figures these vectors are hard to resolve, the general

nature of the flow is clear. This visualization seemed to be better than streamlines, particularly when isolated portions of the flow were magnified.

Foreshadowing the sections which follow, in §2 we present brief details of the problem formulation and our numerical technique. In order to test the numerical method we show in §3 calculations of steady flow past a backward-facing step, comparing our results with existing observations. In §4 we consider the original problem of Sobey (1985), oscillatory flow past a backward-facing step, and compare our calculations with his original observations. The results of calculating flow in a mixing chamber follow in §5. Our conclusions are presented in §6.

2. Numerical model

In order to model vortex wave flows we considered unsteady incompressible flow in two channel geometries which are illustrated in figure 1. One is a simple backward-facing step and the other is a mixing-chamber-type channel. The general situation with which we are concerned is motion of a fluid with kinematic viscosity ν due to a piston of area A_p oscillating with frequency Ω over a stroke k, combined with a mean flow Q. These two motions are fed into a channel of maximum height h and width w. In this case we can define a peak velocity

$$U_0 = \frac{3(A_p \pi \Omega k + Q)}{2wh}. \tag{1}$$

If we non-dimensionalize the velocity by U_0, length by h and the pressure by ρU_0^2 (where ρ is the fluid density), then there are two non-dimensional parameters left in the momentum equations, a Reynolds number $Re = U_0 h/\nu$ and a Strouhal number $St = \Omega h/U_0$. The incompressible flow is then given by a continuity equation

$$\nabla \cdot \boldsymbol{u} = 0 \tag{2}$$

and a momentum equation

$$St\frac{\partial \boldsymbol{u}}{\partial t} + (\boldsymbol{u}\cdot\nabla)\boldsymbol{u} = -\nabla p + \frac{1}{Re}\nabla^2 \boldsymbol{u}. \tag{3}$$

Since we are considering a steady mean component of the flow there is an additional non-dimensional parameter which enters via the boundary conditions at the inlet to the channel. We define the parameter

$$\epsilon = \frac{A_p \pi \Omega k}{A_p \pi \Omega k + Q} \tag{4}$$

so that $\epsilon = 1$ represents purely oscillatory flow while $\epsilon = 0$ imposes no unsteadiness. For purposes of comparison, note that in this paper the Reynolds number is three times that of Sobey (1985) and the Strouhal number is $\frac{16}{3}$ times as great. No-slip boundary conditions are imposed on channel walls and the inlet flow above the step is approximated by quasi-steady flow so that

$$u(0, y, t) = 2[1 - 16(y - \tfrac{3}{4})^2][(1-\epsilon) + \epsilon \sin(2\pi t)]; \quad v = 0, \tag{5}$$

where the channel width is $0 \leqslant y \leqslant 1$. This approximation is valid at the range of frequencies we are considering. The outlet boundary conditions are the same as in Hagstrom (1990),

$$\frac{\partial v}{\partial x} = 0, \quad p - \frac{1}{Re}\frac{\partial u}{\partial x} = 0. \tag{6}$$

In order to visualize the numerical results we plot velocity vectors at points in the flow domain. These are scaled to approximate photographic traces which might be

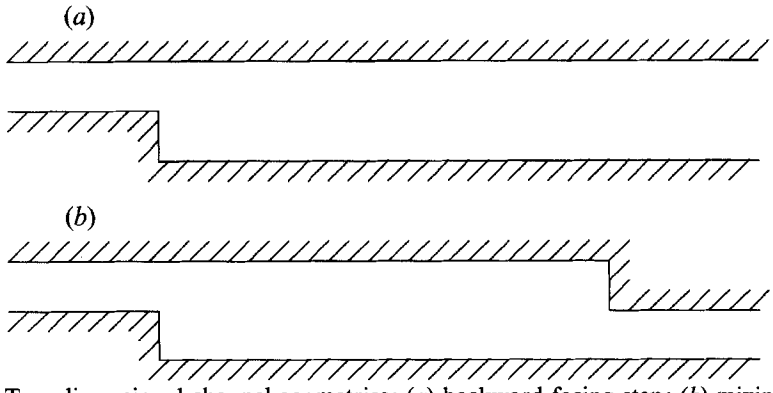

FIGURE 1. Two-dimensional channel geometries: (*a*) backward-facing step; (*b*) mixing chamber.

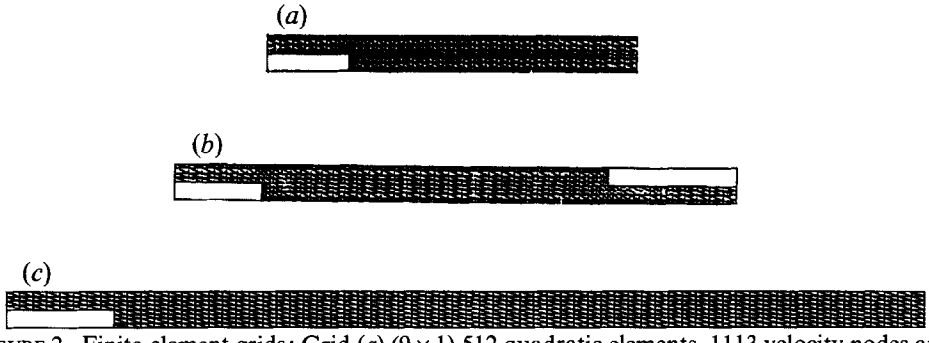

FIGURE 2. Finite-element grids: Grid (*a*) (9 × 1) 512 quadratic elements, 1113 velocity nodes and 301 pressure nodes; Grid (*b*) (13 × 1) 672 quadratic elements, 1465 velocity nodes and 397 pressure nodes; Grid (*c*) (26.5 × 1) 1024 quadratic elements, 2201 velocity nodes and 589 pressure nodes.

observed in an experiment using water with a camera shutter speed of $\frac{1}{120}$th of a second in a channel of width 2 mm. The numerical solution involves an implicit θ-method time discretization of the transient, incompressible Navier–Stokes equations. Spatial discretization is accomplished by a Galerkin finite-element formulation. The method chosen applies quadratic basis functions for velocity and linear basis functions for pressure. Triangular elements were used to provide flexibility in the domain construction. The Navier–Stokes convection terms are linearized via Picard linearization and a preconditioned bi-conjugate gradient linear solver is used in the method of solution. Further detailed information regarding the numerical method can be found in DeBlois (1991). Various numerical results were obtained on the grids depicted in figure 2. These grids were chosen as a result of a series of mesh-refinement numerical experiments. We discuss this briefly in the conclusions of this paper.

3. Steady flow over a backward-facing step

In order to validate the numerical algorithm we have compared the calculated results with experiment for steady and unsteady flows and considered the effect of mesh refinement. In this section we describe the comparison of our numerical results against observations of steady flows past a backward-facing step. Comparisons against observations of unsteady flow are also given in §4 and additional validation by mesh refinement is described in §6.

Steady two-dimensional flow over a backward-facing step is a well-established

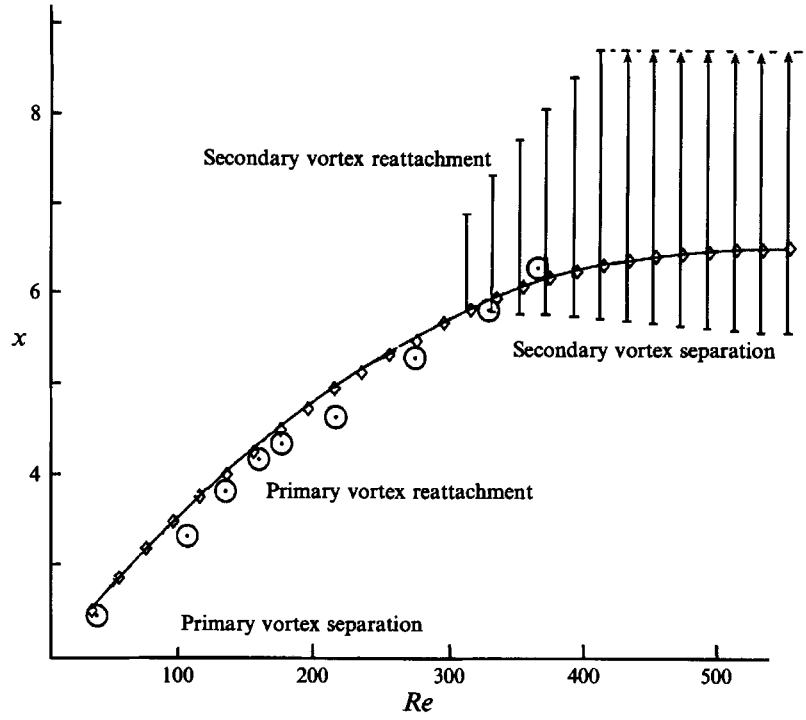

FIGURE 3. Vortex length over a backward-facing step: ◇, DeBlois (1990) (quadratic finite elements, 2527 DOFs); ⊙, Sobey (1985) (laboratory observations).

problem for which there are many experimental observations. Flow separates in the lee of the channel expansion and the primary vortex increases with increasing Reynolds numbers. Secondary vortices form on the opposite wall, and their length is also Reynolds number dependent. Laboratory observations show that at high Reynolds numbers (> 700) the flow quickly becomes three-dimensional and ultimately unstable. However, in the range below $Re = 700$ observations show that a steady two-dimensional flow exists (Cherdron, Durst & Whitelaw 1978; Armaly *et al.* 1983; and Sobey 1985). Our numerical solutions agree with observations over this low Reynolds number range and are illustrated in figure 3, where we show primary vortex length, the position of the secondary vortex, and the observations of Sobey (1985). The close agreement, along with h-refinement error estimates, gives us confidence that the numerical algorithm is able to adequately resolve flow features of interest.

4. Unsteady flow over a backward-facing step

We now consider purely oscillatory flow ($\epsilon = 1$) past a backward-facing step and investigate the deceleration phase as $t \to \frac{1}{2}$. Ralph (1986) found that in cylindrical geometries there were parameter ranges for which the decelerating flow depended on the previous half-cycle and so the initial half-cycle was not always typical of subsequent half-cycles. Our calculations have shown that in the parameter range we are considering the flow during the deceleration of the first half-cycle (which started from rest) is a good approximation to flow in the deceleration phases of subsequent half-cycles. The independence of the flow in our parameter range from its starting conditions has been observed by Sobey (1980) and Bittleston (1986), in each case for laminar two-dimensional flow. The formation of a vortex wave is illustrated in figure

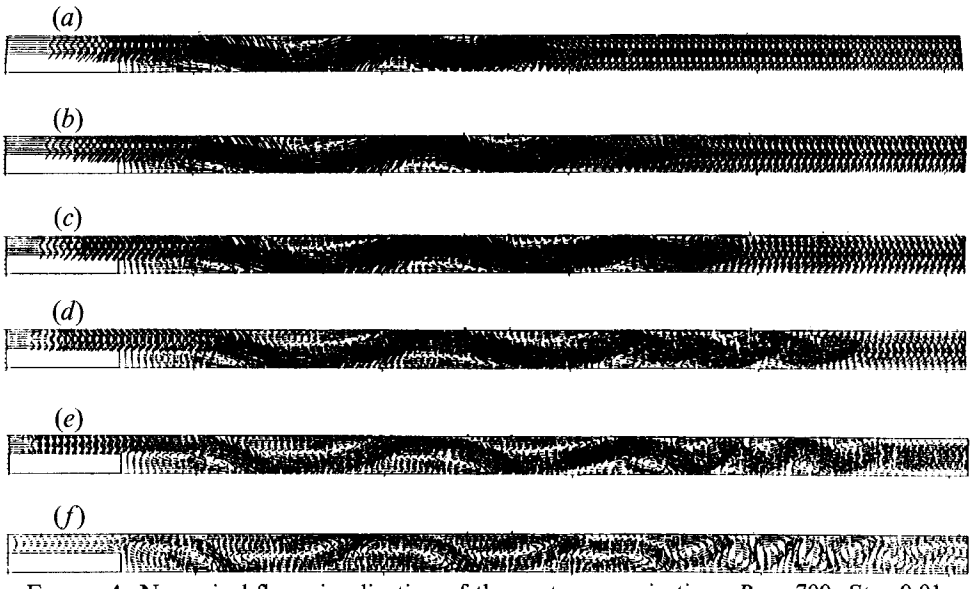

FIGURE 4. Numerical flow visualization of the vortex wave in time, $Re = 700$, $St = 0.01$: (*a–f*) $t = 0.25, 0.3, 0.35, 0.4, 0.45, 0.5$; $\epsilon = 1$, and channel length = 26.5.

4 where we show a sequence in time of flow at a Reynolds number of 700 and a Strouhal number of 0.01. These results match the development in time shown by the experiments of Sobey (1985). It can be seen that at peak flow the dominant vortex is not the primary vortex which formed in the lee of the channel expansion but rather the secondary vortex which developed on the opposite wall. Were the flow development to be quasi-steady then at this Reynolds number the secondary vortex should be very weak. Obviously, the significance of unsteadiness is shown by the size of the secondary vortex. In this case there is already a substantial vortex wave formed at peak flow and this supports the results of Stephanoff *et al.* (1983) and Sobey (1985) that the vortex wave originates in an inviscid deformation of a rotational core flow. In Sobey (1985) it was shown that an asymptotic theory based on that idea led to a rapidly decaying wave-like structure within steady flow through an asymmetric channel and the presence of a wave at peak flow lends support to that theory. Further support will emerge shortly.

Another feature which is apparent and has not been commented on before is the distinct change of wavelength evident in figures 4(*e*) and 4(*f*). Re-examination of the photographs in Sobey (1985) confirm that this feature also occurs in experiments and may indicate the existence of two different wave structures within the vortex wave.

The initial wave, which has a relatively long wavelength (3–4 times the channel width), is probably the wave predicted by long-wavelength inviscid deformation of the core flow, as in Stephanoff *et al.* (1983) and Sobey (1985). The second wave, where the wavelength is comparable with the channel width, may in fact arise from a free boundary-layer interaction as suggested by Bogdanova & Ryzhov (1983). This would resolve the question of how these two different mechanisms for producing a wave structure interact.

Since the wave calculated in figure 4(*f*) reaches the end of the numerical domain, we recomputed the solution over a much longer domain to ensure that the numerical result was not corrupted by a reflected boundary condition. The result was that parallel flow developed immediately beyond the end of figure 4(*f*).

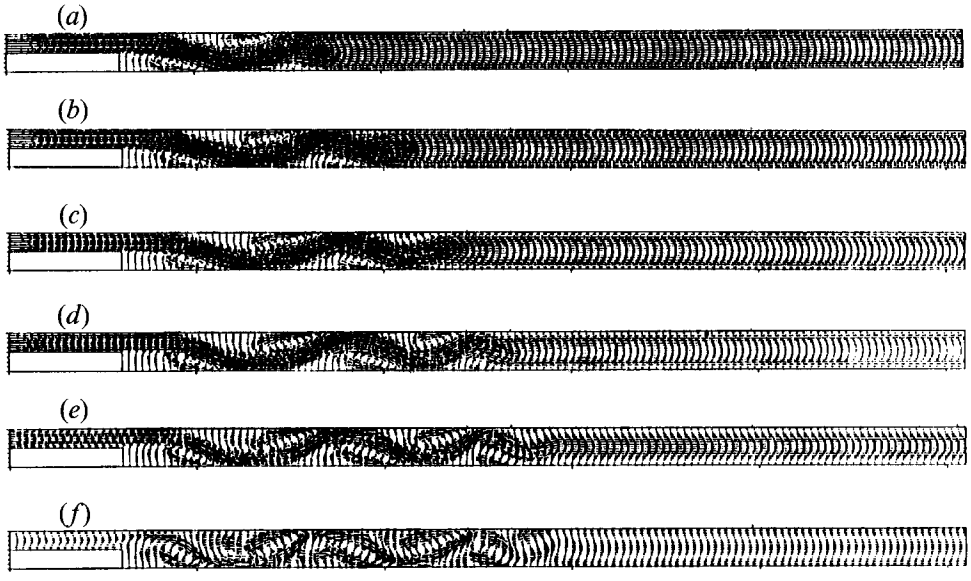

FIGURE 5. Numerical flow visualization of the vortex wave in time, $Re = 700$, $St = 0.02$: (*a–f*) $t = 0.25, 0.3, 0.35, 0.4, 0.45, 0.5$; $\epsilon = 1$, and channel length = 26.5.

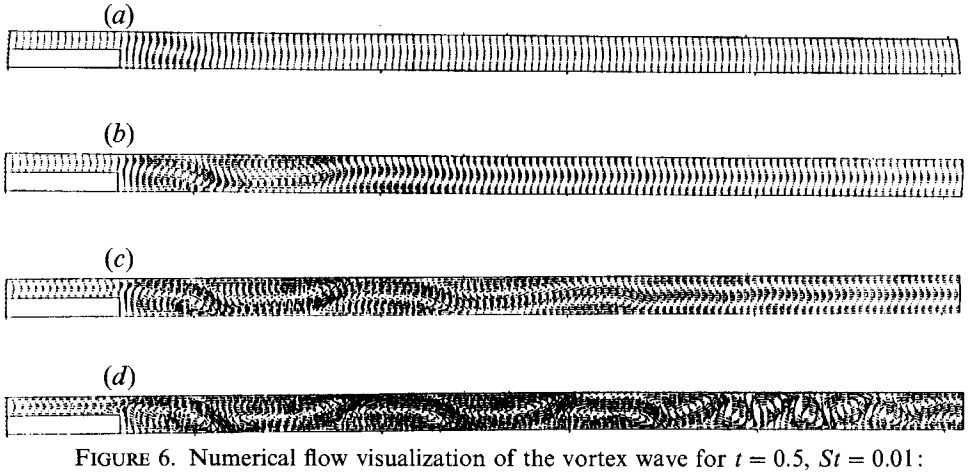

FIGURE 6. Numerical flow visualization of the vortex wave for $t = 0.5$, $St = 0.01$: (*a–d*) $Re = 250, 400, 550, 700$; $\epsilon = 1$, and channel length = 26.5.

If the Strouhal number is increased to 0.02, then a time sequence (figure 5) again shows the same features as observed by Sobey (1985). The wavelength has decreased and so too has the longitudinal extent of the vortices. In this case it is also evident that a change of wavelength occurs (figure 5*f*), although here the second wave structure is damped very rapidly.

In order to further characterize the vortex wave we have calculated flows at fixed Strouhal numbers and varying Reynolds numbers. We summarize these results by plotting only the flow at $t = 0.5$, the instant of mean flow reversal. In figure 6 the Strouhal number is fixed at 0.01 and it can be seen that as in Sobey (1985) there is a dramatic increase in longitudinal extent of the wave as the Reynolds number is increased.

One other feature apparent from our calculations concerns vortex splitting or eddy

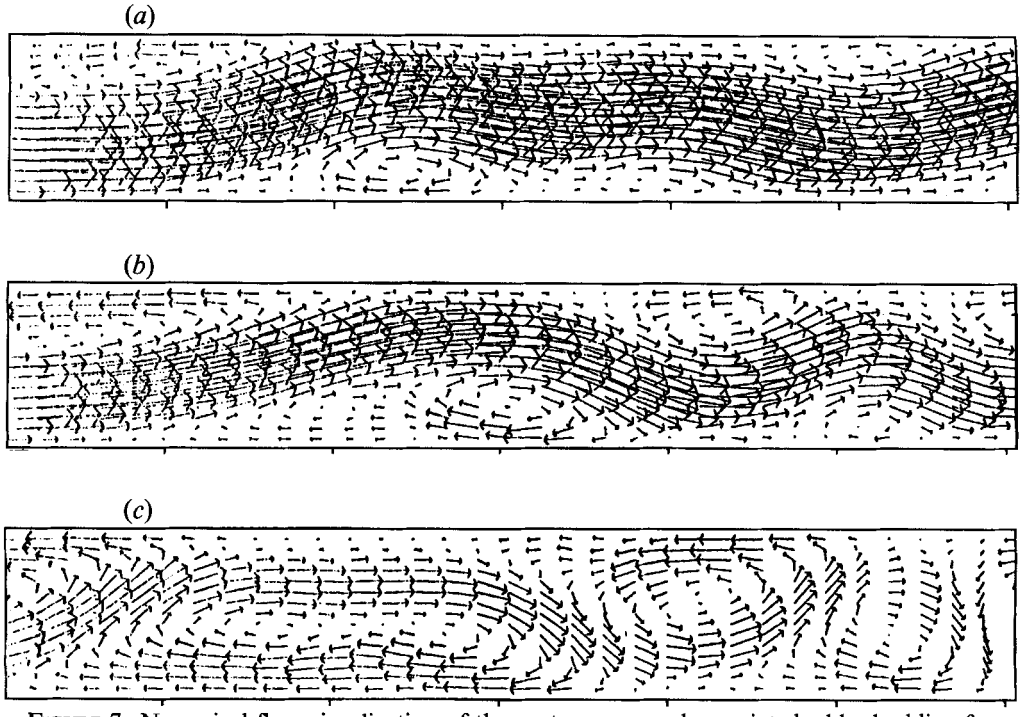

FIGURE 7. Numerical flow visualization of the vortex wave and associated eddy doubling for $Re = 700$, $St = 0.01$: (*a–c*) $t = 0.4$, 0.45, 0.5; and $\epsilon = 1$.

doubling. This formation of co-rotating vortices has been discussed by Pedley & Stephanoff (1985) and Ralph & Pedley (1988) where they find eddy doubling predicted by long-wavelength asymptotic analysis and for calculations of steady flow past a moving indentation. Our calculations of eddy doubling are illustrated in figure 7 where we show an expanded view of a section of figure 4(*d–f*). It is clear that eddy doubling is evident in figure 7(*a*) but that the subsequent development in time (figure 7*b*, *c*) is the result of very rapid transients. We do not believe that it has been suggested that eddy doubling might be a highly transient process within the overall oscillating flow. Since existing asymptotic analyses are for long-wavelength low-frequency disturbances it is not surprising that this has not been suggested before. The calculations presented in figure 7 certainly warrant further numerical and asymptotic examination. In this context it is worth noting that the theory of Bogdanova & Ryzhov (1983) predicts disturbances from a free boundary-layer interaction which indeed are of very high frequency (see Sobey 1985, p. 423 and Smith & Burggraf 1985 who have considered short-scale disturbances to boundary layers).

5. Unsteady flow in a mixing chamber

We now continue our examination of the vortex wave in a mixing chamber. Although strong waves at high Reynolds numbers are evident in §4, many applications, such as those involving blood, are shear-limited (i.e. fluid constituent particles cannot withstand high shear forces), so many applications of the vortex wave may be suited to flows with low characteristic Reynolds numbers. Thus a mapping of the vortex wave over an *Re–St* domain at lower Reynolds numbers was pursued. These results also strengthen the conclusions drawn from the previous section.

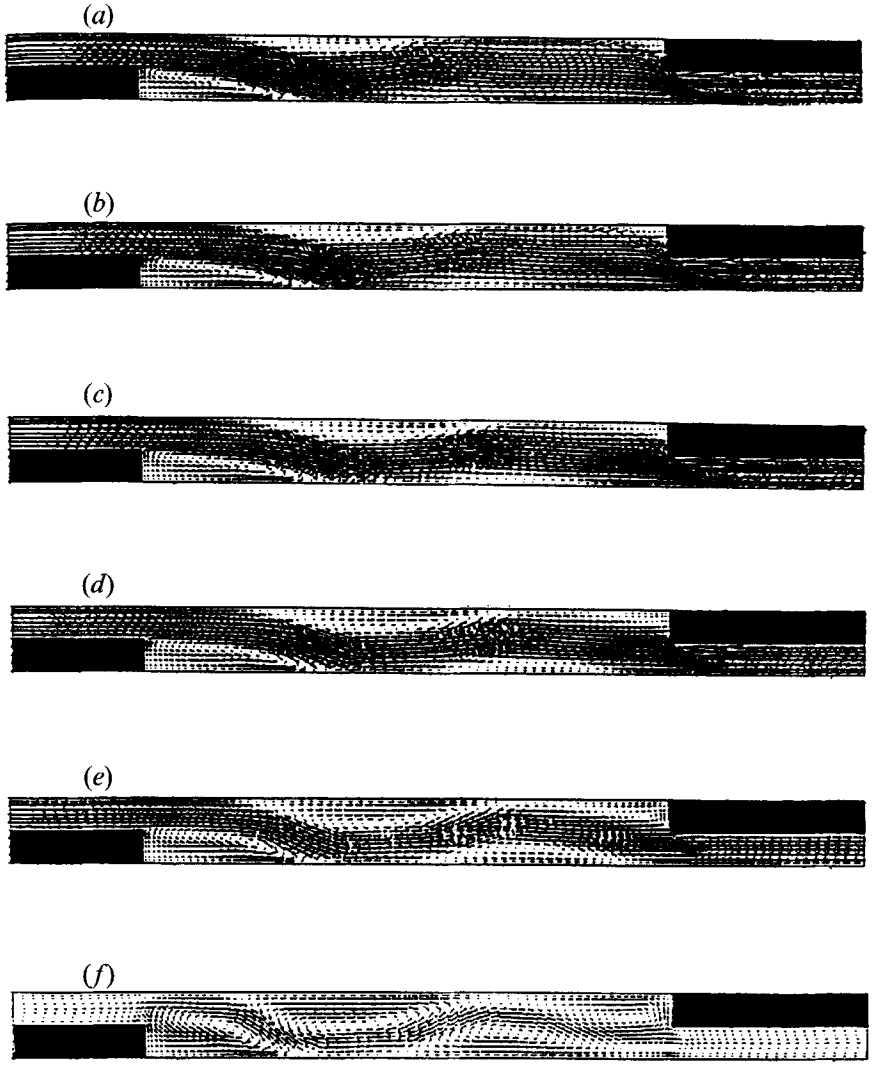

FIGURE 8. Numerical flow visualization of the vortex wave in time, $Re = 300$, $St = 0.02$: (*a–f*) $t = 0.25, 0.3, 0.35, 0.4, 0.45, 0.5$; $\epsilon = 1$, deflector spacing = 8, and channel length = 13.

The 13×1 numerical grid shown in figure 2(*b*) was implemented over a $200 \leqslant Re \leqslant 400$ by $0.01 \leqslant St \leqslant 0.06$ domain. Mesh refinement in the potential problem areas of pressure singularities (deflector corners) and concentration boundary layers (wall effects) are apparent. 36 numerical experiments were accomplished to establish the character of the vortex wave over this *Re–St* domain, for the particular circumstance of $\epsilon = 1$, deflector spacing = 8, a sinusoidal pulse, and rectangular obstructions. Figure 8 is another example of the development of the vortex wave in the deceleration phase of pulsatile flow for a Reynolds number of 300 and Strouhal number of 0.02. As in §4, these results also match the development in time demonstrated by the experiments of Sobey (1985). For these parameters and most of those covering the chosen *Re–St* domain, the wave does not fully develop until the latter phases of deceleration (around $t = 0.4$). This is unlike the higher Reynolds' number results of §4, and is primarily an effect of low Reynolds number. From peak flow ($t = 0.25$) to the latter stage of

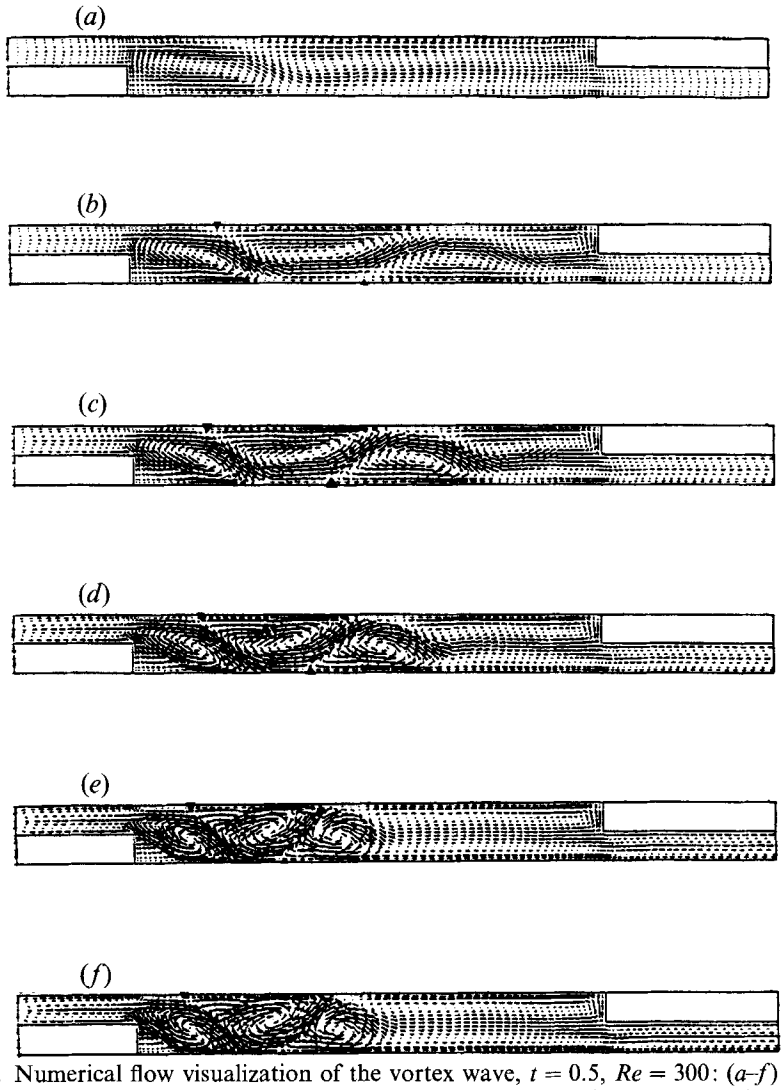

FIGURE 9. Numerical flow visualization of the vortex wave, $t = 0.5$, $Re = 300$: (a–f) $St = 0.01$, 0.02, 0.03, 0.04, 0.05, 0.06; $\epsilon = 1$, deflector spacing = 8, and channel length = 13.

deceleration, the secondary separation on the top wall is observed to dominate the character of the flow, confirming the significance of unsteadiness already mentioned.

As with the results of the previous section, the clearest picture of the vortex wave is observed at zero flow (e.g. figure 8f), which is why we chose this 'snap-shot' to visualize different waves. Using this characterization, in figure 9 the Reynolds number is fixed at 300 and the Strouhal number is allowed to vary, while in figure 10 the Strouhal number is fixed at 0.03 and the Reynolds number is allowed to vary. The overriding conclusion drawn from figures 9 and 10 (as well as figure 6) is that while the Reynolds number (pulse stroke length and frequency) determines the number of vortices and their strength, the Strouhal number (stroke length only) dictates the wavelength (λ). Asymptotic analyses summarized in Sobey (1985) predict a very weak λ-dependence upon Reynolds number ($l \propto Re^{-\frac{1}{7}}$) but a stronger λ-dependence upon Strouhal number ($\lambda \propto St^{-\frac{1}{3}}$). The weak dependence of λ upon Reynolds number is reflected in figure 10 as well as in figure 6, where a fixed Strouhal number and varying

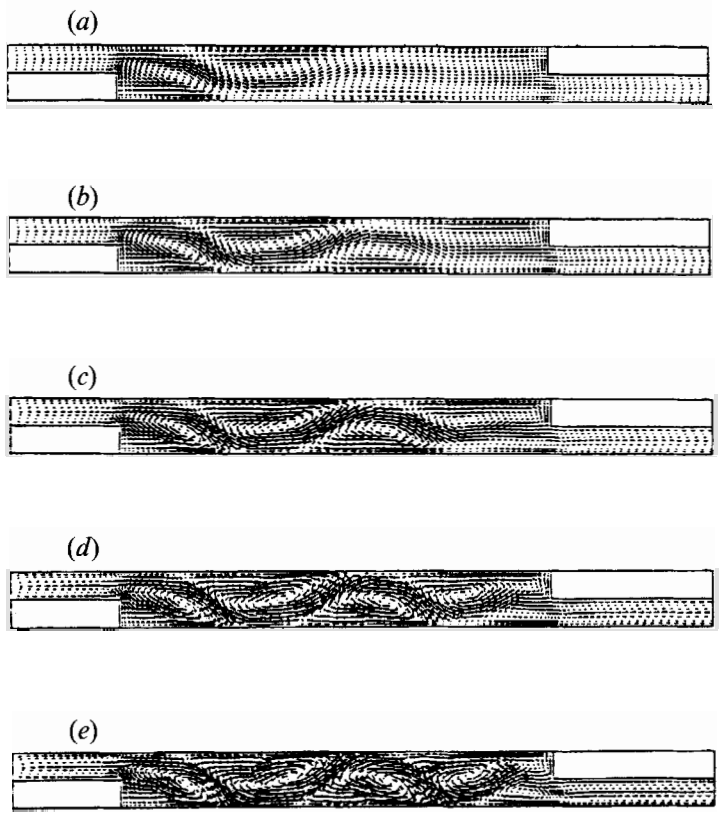

FIGURE 10. Numerical flow visualization of the vortex wave, $t = 0.5$, $St = 0.03$: (*a–e*) $Re = 200$, 250, 300, 350, 400; $\epsilon = 1$, deflector spacing = 8, and channel length = 13.

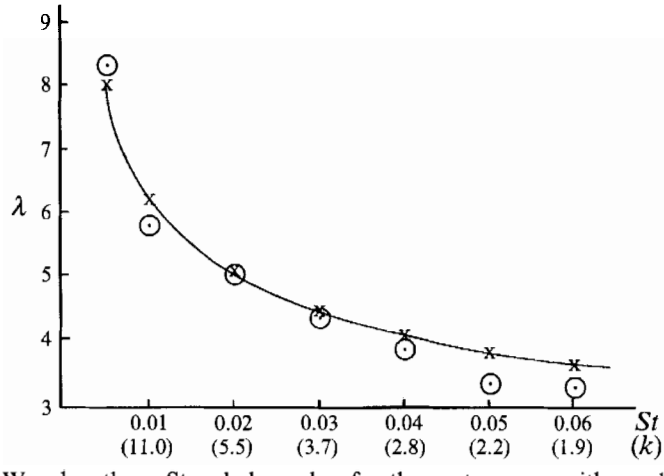

FIGURE 11. Wavelength *vs.* Strouhal number for the vortex wave with $\epsilon = 1$: ⊙, numerical result; — × —, asymptotic expectation.

Reynolds number causes very little change in wavelength. A strong λ-dependence on Strouhal number is indicated by a decreasing λ with increasing Strouhal number obvious in figure 9. In figure 11 we combine the numerical results of figures 4, 5 and 9 and plot them against the asymptotic expectation of $\lambda \propto St^{-\frac{1}{3}}$ to confirm the latter.

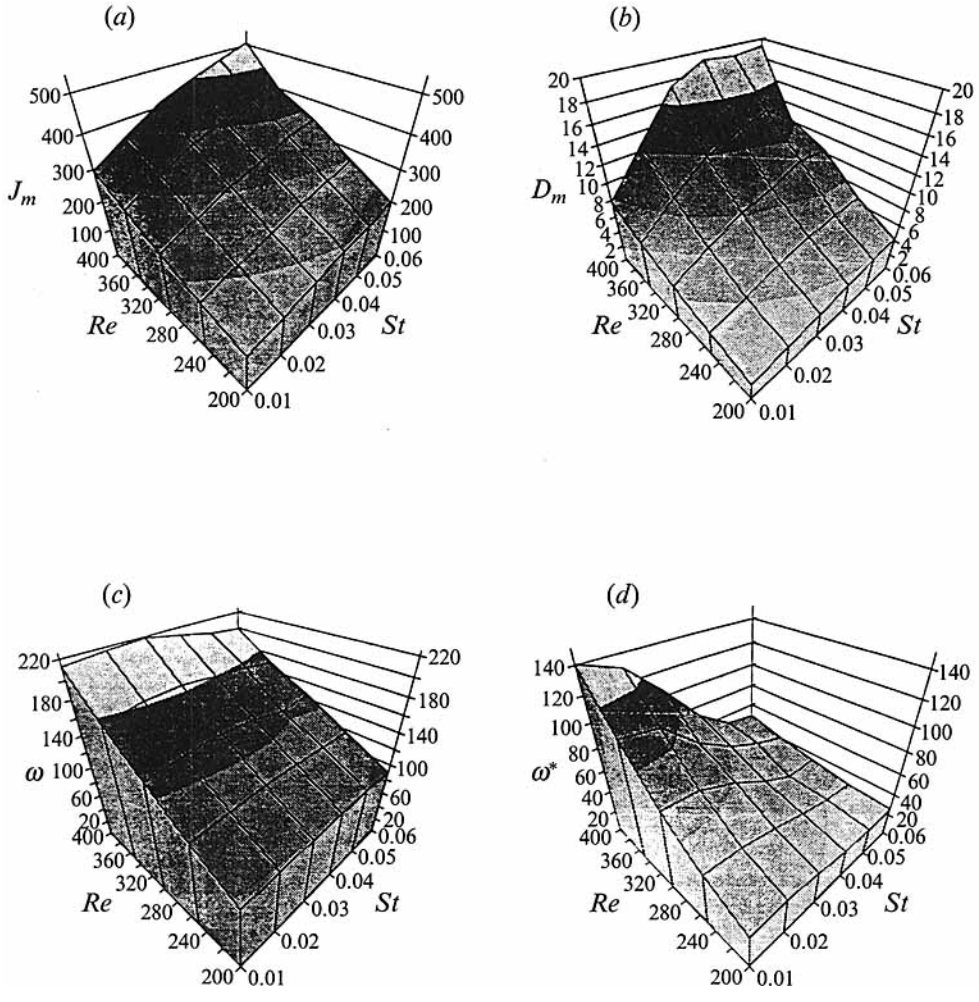

FIGURE 12. (*a*) Average horizontal wall shear (J_m); (*b*) average increase in diffusivity (D_m scaled to 1×10^{-4}); (*c*) average nodal vorticity (ω); (*d*) average, dispersion-weighted nodal vorticity (ω^*) due to the vortex wave; $\epsilon = 1$, deflector spacing = 8, and channel length = 13.

Figure 11 also includes a result at $Re = 800$, $St = 0.005$ not visualized in any of the previous figures.

With regard to mixing applications, the vortex wave has two fundamental effects on fluid flow. The first of these is an alteration of the flow local to the channel walls, which in application could reduce material buildup there. To quantify these local effects we define

$$J_m = \int_{wall} \frac{\partial u}{\partial y} \mathrm{d}x \quad \text{(average horizontal wall shear)}, \tag{7}$$

and

$$D_m = \int_{wall} \left(\frac{\partial v}{\partial y} [\delta y]^2 \right) \mathrm{d}x \quad \text{(average additional tendency to diffuse)}. \tag{8}$$

Averages are accomplished spatially on the walls between deflectors and temporally through one pulse cycle.

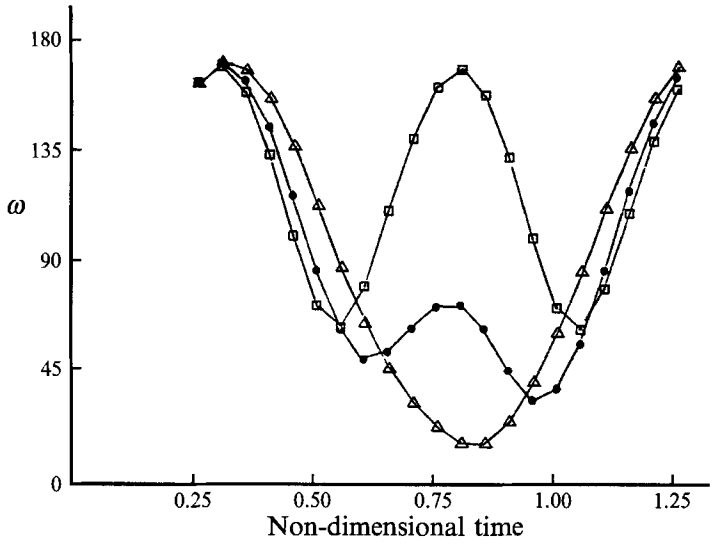

FIGURE 13. Nodal vorticity ω through one pulse cycle for $Re = 250$, $St = 0.03$, various ϵ values, deflector spacing = 8, and channel length = 13. △, $\epsilon = 0.5$, $\bar{\omega} = 91.4$; ●, $\epsilon = 0.75$, $\bar{\omega} = 90.7$; □, $\epsilon = 1.0$, $\bar{\omega} = 119.2$.

The second effect of the wave on fluid flow is a global mixing effect as opposed to the local wall effects. In order to quantify the total mixing effect of a vortex wave, we define throughout the domain

$$\omega = \iint \left(\frac{\partial v}{\partial x} - \frac{\partial u}{\partial y}\right) \mathrm{d}y\,\mathrm{d}x \quad \text{(average vorticity)}, \tag{9}$$

and

$$\omega^* = \omega \left(2\frac{N_A}{N_T}\right)^5 \quad \text{(average dispersion weighted vorticity)}, \tag{10}$$

where N_T represents the total number of nodes and N_A is the number of nodes with ω values greater than the mean. Here the averages are accomplished spatially within the domain and temporally through one pulse cycle.

Using these measures to compare 36 different vortex waves over the chosen *Re–St* domain, we plot the results in figure 12. Several observations can readily be made. Higher Strouhal numbers and fixed Reynolds numbers are produced by shortening the stroke length and increasing the pulse frequency (equation (1)). This produces a more energetic wave of shorter wavelength, consistent with previous findings. Vorticity seems to be independent of Strouhal number (figure 12*c*), implying that the total channel vorticities of figures 9(*a–f*) are equivalent. Recognizing that total mixing would be better served by less violent, more dispersed vortices, we produced a dispersion-weighted vorticity to account for this. Figure 12(*d*) demonstrates this, indicating, for instance, that the wave in figure 9(*c*) is a better means of mixing the flow than the wave in figure 9(*f*). Note that Sobey (1985) also predicted a more extended vortex wave with increasing Reynolds number and decreasing Strouhal number.

As a further means of examining the vortex wave, we examined the durability of the wave when corrupted by additional factors such as a superimposed bulk flow, a change of pulsation type, various deflector spacings and shapes, and the imposition of wall suction. Figure 13 uses the vorticity quantifier plotted in time through one pulse cycle to demonstrate the effect of a superimposed bulk flow on a pulsating flow. $\epsilon = 1$ shows

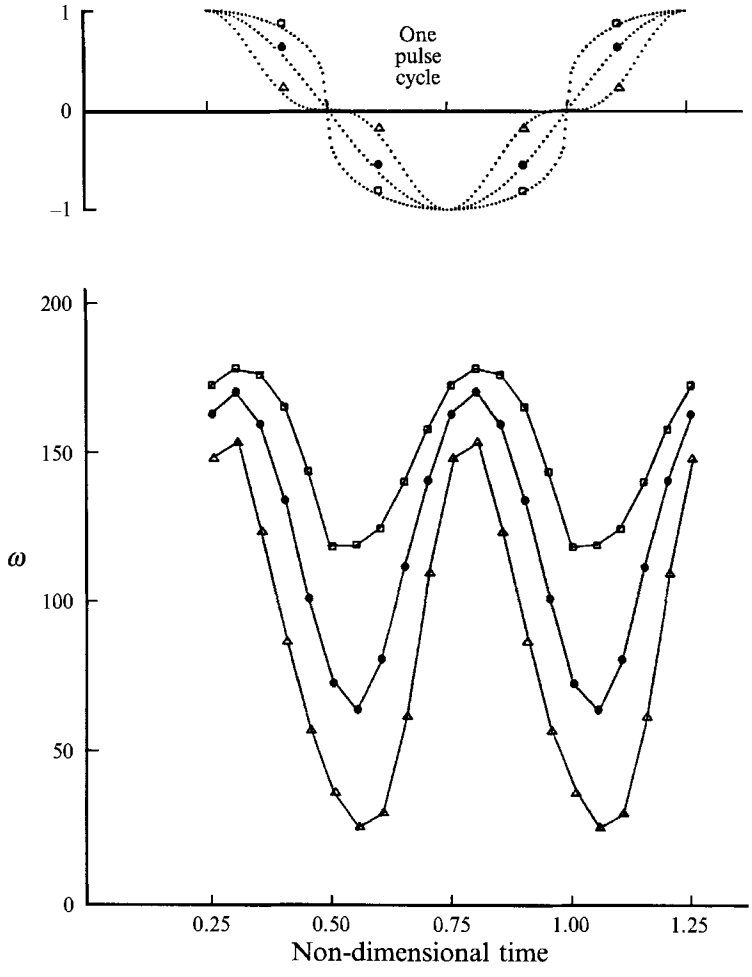

FIGURE 14. Nodal vorticity ω through one pulse cycle for $Re = 250$, $St = 0.03$, various pulsed flows: □, $\sin^{\frac{1}{3}}$, pulsation, $\bar{\omega} = 149.8$; ●, $\sin^{1}$, $\bar{\omega} = 119.2$; △, $\sin^{3}$, $\bar{\omega} = 83.6$. $\epsilon = 1$, deflector spacing = 8, and channel length = 13.

symmetry in the half-cycle, confirming the experimental observations at these lower Reynolds numbers that for full pulsation a wave develops in the deceleration of forward flow, is washed away in the acceleration of reverse flow, and a new wave develops in the deceleration of the reverse flow. If part of the forward flow is considered to be a bulk flow, the wave in the forward direction is not impeded significantly, but the bulk flow will impede the reverse flow and subsequently the vortex wave in that direction. An industrial requirement of high mean flow will prevent the formation of a vortex wave in the reverse direction. The results do suggest a compromise. If flow is initially decelerated very closely (maintaining high mean flow), and then decelerated very quickly to get the pulsation close to $\epsilon = 1$, the result may be a complementing rather than a competing effect of both higher sustained flow and a stronger pulsation. Rotating a piston arm through an elliptical path as opposed to a circular path (sinusoidal pulsation) could yield the desired effect. Figure 14 compares a quicker deceleration ($\sin^{\frac{1}{3}}$) to both the sinusoidal pulse used so far and to a slower decelerating pulse ($\sin^{3}$). The faster decelerating pulse yielded the following improvements over the sinusoidal pulse: $J_m + 24\%$, $D_m + 12\%$, $\omega + 26\%$, and $\omega^* + 37\%$.

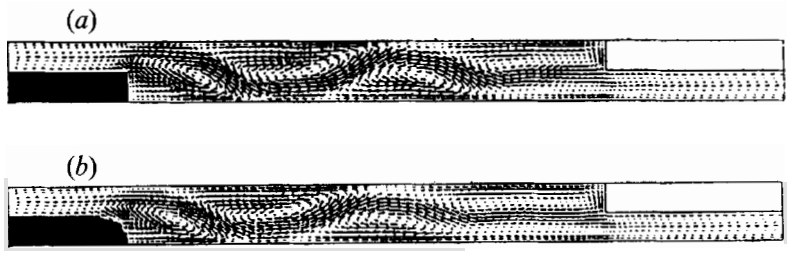

FIGURE 15. Numerical flow visualization of the vortex wave for different shaped deflectors, $Re = 300$, $St = 0.03$, $\epsilon = 1$, deflector spacing = 8, and channel length = 13.

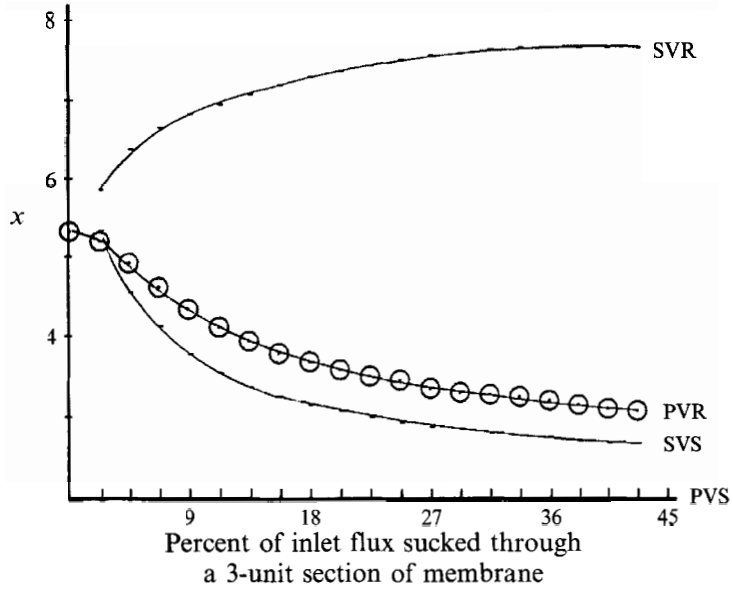

FIGURE 16. Vortex length reduction due to transverse wall suction. PVS(R), primary vortex separation (reattachment); SVS(R), secondary vortex separation (reattachment).

In addition to variations of the pulse, we also considered variations of deflector spacing and shape. All four quantifying measures showed that upstream vortices were significantly stronger than downstream vortices and the application of the vortex wave in channels which allowed two or three vortices maximized mixing. The importance of an abrupt expansion ratio is indicated by the numerical experiment portrayed in figure 15. A slight modification to the upstream obstruction initiated the wave further upstream and caused the following reduction in the four measures: $J_m - 16\%$, $D_m - 25\%$, $\omega - 9\%$, and $\omega^* - 2\%$.

Finally, several applications of the vortex wave occur in cross-flow filtration processes, so we consider here the effect of wall suction on vortex length. For steady flow over a backward-facing step, we constructed a membrane extending from the base of the step three units downstream (6 times the height of the step). We then varied the percentage of inlet flux sucked through this membrane and continuously measured the length of the vortex. The results are depicted in figure 16. For some applications, high suction may inhibit the wave, but to keep these results in perspective, a typical filtration device filters about 10% of the bulk flow over an entire 80×2 membrane surface. This

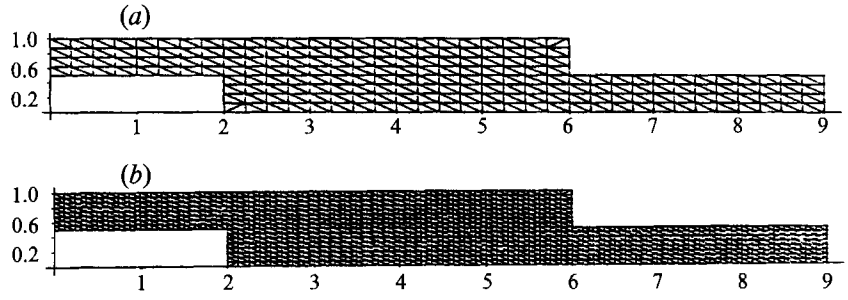

FIGURE 17. Quadratic, triangular-element numerical grids: (*a*) coarse grid – 921 velocity nodes, 253 pressure nodes, and 416 elements; (*b*) fine grid – 3503 velocity nodes, 921 pressure nodes, and 1664 elements.

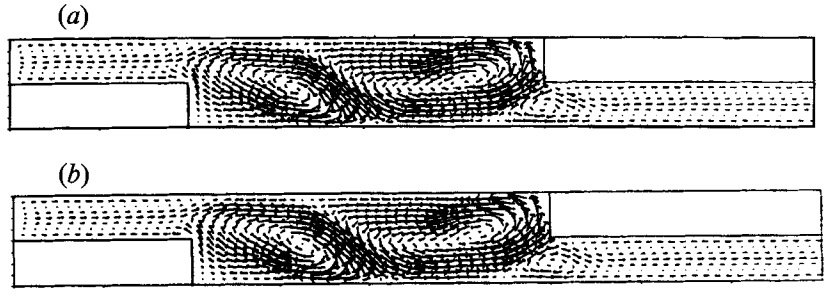

FIGURE 18. Pulsatile flow for $Re = 300$, $St = 0.03$, arrow length $= \frac{1}{120}$ s × local velocity: (*a*) coarse grid solution; (*b*) fine grid solution.

equates to negligible suction velocities due to only about 0.2% of the inlet flux being sucked through 3 unit portions of a membrane. Figure 16 indicates at that level, wall suction velocities are simply too small to affect vortex length, and hence a vortex wave.

6. Conclusions

Results of §3 confirmed the numerical steady flows and thus far laboratory observations have been used to justify interpreting these results as accurate. In addition to this we pursued an *a posteriori* h-refinement error estimate to validate the transient results. The two regular quadratic, finite-element grids shown in figure 17 were used. The coarse mesh is typical of the grids used throughout this paper while the fine grid is a 4 to 1 refinement. Purely pulsatile flow ($\epsilon = 1$) with $Re = 300$ and $St = 0.03$ was calculated on both meshes. A zero-flow visualization at $t = 0.5$ is plotted in figure 18. For comparison, only the solution vectors on the fine mesh which correspond to those on the coarse mesh are plotted. Visually, there is no significant difference between the two solutions. Quantitatively, the average nodal difference through an entire pulse cycle was less than 2.5%. The Taylor–Hood finite element used is known to have a convergence rate of $O(h^3)$. Given a 2.5% average nodal difference between the coarse $O(\frac{1}{16}^3)$ and fine $O(\frac{1}{32}^3)$ grids, it seems that both solutions are in the tail of convergence and a consistent numerical approximation is obtained. Given this numerical evidence and the experimental observations of Sobey (1985), the results of this paper can be interpreted as accurate.

The significance of unsteadiness in the generation of the vortex wave has been emphasized and our numerical results demonstrate a change in downstream

wavelength. We have suggested that the vortex wave is an interaction of an inviscid deformation of a rotational core flow causing the upstream long wavelength (predicted by Stephanoff *et al.* 1983) while a free boundary-layer interaction is responsible for the high-frequency downstream wave (predicted by Bogdanova & Ryzhov 1983). Eddy doubling (predicted by Ralph & Pedley 1988) seems to be a highly transient product of this interaction. We have also confirmed the $\lambda \propto St^{-\frac{1}{3}}$ relation summarized in an asymptotic analysis presented in Sobey (1985) and we have numerically verified Sobey's observations that stronger and more extended waves occur at higher Reynolds number and lower Strouhal numbers. Applications of the vortex wave to high mean flow situations requires quick decelerations, short deflector spacings and abrupt expansion ratios. Finally, for the specific applications to cross-flow filtration, the wave is not affected by realistic filtration velocities.

B. DeBlois would like to acknowledge the support of the Seiler Research Laboratory, USAF Academy, CO USA and S. Alani would like to acknowledge support from SERC.

REFERENCES

AMALY, B. F., DURST, F., PEREIRA, J. & SCHULTEN, B. 1983 Experimental and theoretical investigation of backward-facing step flow. *J. Fluid Mech.* **127**, 315.

BELLHOUSE, B. J. & LEWIS, R. W. H. 1988 A high efficiency membrane separator for donor plasmapheresis. *Trans. Am. Soc. Artificial Internal Organs* **34**, 747.

BITTLESTON, S. H. 1986 Flows past arrays of cylinders. PhD dissertation, Bristol University.

BOGDANOVA, E. V. & RYZHOV, O. S. 1983 Free and induced oscillations in Poiseuille flow. *Q. J. Mech. Appl. Maths* **36**, 271.

CHERDRON, W., DURST, F. & WHITELAW, J. H. 1978 Asymmetric flows and instabilities in symmetric ducts with sudden expansions. *J. Fluid Mech.* **84**, 13.

DEBLOIS, B. M. 1991 The vortex wave with applications to cross-flow filtration. PhD dissertation, Oxford University Numerical Analysis Group.

DEBLOIS, B. M. & SOBEY, I. J. 1992 Quadratic upwinded finite element solution to the transient incompressible Navier–Stokes' equations (in preparation).

HAGSTROM, T. 1990 Conditions at the downstream boundary for simulations of viscous incompressible flow. *NASA Tech. Memo 102510.* (ICOMP-90-05).

PEDLEY, T. J. & STEPHANOFF, K. D. 1985 Flow along a channel with a time-dependent indentation in one wall: the generation of vorticity waves. *J. Fluid Mech.* **160**, 337.

RALPH, M. E. 1986 Oscillatory flows in wavy-walled tubes. *J. Fluid Mech.* **168**, 515.

RALPH, M. E. & PEDLEY, T. J. 1988 Flow in a channel with a moving indentation. *J. Fluid Mech.* **190**, 87.

SMITH, F. T. & BURGGRAF, O. R. 1985 On the development of large-sized, short-scaled disturbances in boundary layers. *Proc. R. Soc. Lond.* A **399**, 25.

SOBEY, I. J. 1980 On flow through furrowed channels. Part 1. Calculated flow patterns. *J. Fluid Mech.* **96**, 1.

SOBEY, I. J. 1985 Observations of waves during oscillatory channel flow. *J. Fluid Mech.* **151**, 395.

STEPHANOFF, K. D., PEDLEY, T. J., LAWRENCE, C. J. & SECOMB, T. W. 1983 Fluid flow along a channel with an asymmetric oscillating constriction. *Nature* **305**, 692.

TUTTY, O. R. & PEDLEY, T. J. 1992 Pulsatile flow in a constricted channel. *J. Biomech. Engng* (submitted).